Proceedings of ASME Turbo Expo 2011
GT2011
June 6-10, 2011, Vancouver, British Columbia, Canada

GT2011-45429

INVESTIGATION OF GAS COMPOSITION EFFECTS ON THE AEROTHERMAL CHARACTERISTICS OF A FILM-COOLED FLAT PLATE AT HIGH-TEMPERATURE CONDITIONS

Xin Zou **Xin Yuan**
Key Laboratory for Thermal Science and Power Engineering of Ministry of Education
Department of Thermal Engineering
Tsinghua University
Beijing, P. R. China 100084
Email: jux03@mails.tsinghua.edu.cn

ABSTRACT

Both experimental and computational investigations were carried out in this paper to study the influences of turbine inlet steam concentration on turbine flow and heat transfer under high-temperature and pressurized conditions. A high-temperature experimental facility has been built to study the steam concentration effects on turbine aerothermal characteristics for future advanced turbines in IGCC power systems. Preliminary data were obtained from experiment and used to validate the computational models presented in this paper. Results from computational modeling were compared qualitatively with previous studies and also quantitatively with our experimental measurements in this study, both of which proves the validation of the presented computational approach.

Based on the validated computational models, a series of numerical investigations were conducted. Relationship between the change in gas inlet steam concentration and the corresponding change in dimensionless spanwise-averaged heat flux distribution was found to be well correlated with the form of power function. The influence of turbine inlet pressure and temperature on the aerothermal characteristics of turbine heat transfer is also considered and discussed. Finally, an overall correlation based on the numerical investigations were presented, and the capability of this correlation was validated with full CFD computation. The correlation can predict the trend of the dimensionless spanwise-averaged heat flux quite well with an acceptable accuracy.

NOMENCLATURE

$\Delta(\cdot)$	$(\cdot)_{high} - (\cdot)_{low}$
A	surface area
atm	atmospheric pressure
BR	blowing ratio
D	hole diameter
DR	density ratio
F	configuration factor (or view factor)
Ma	Mach number
N	number of surrounding surfaces
p	static pressure
PF	pressure influence factor
Q	net radiation heat transfer
Re	Reynolds number
T	static temperature
t	temperature of thermocouple's measurement junction
TI	turbulence intensity
VR	velocity ratio
X	distance downstream of the hole exit
x	mole fraction
y^+	wall y plus
Greek	
α	streamwise angle
ε	interior surface emissivity of cavity
$\varepsilon(T)$	emissivity of superalloy
η	overall cooling effectiveness, $(T_G - T_W)/(T_G - T_C)$
q''	heat flux

Overbar

$-$	spanwise average
$=$	plate surface area average

Subscripts

$base$	baseline
C	coolant
G	gas
H_2O	steam related variable
$high$	high inlet steam concentration
i, j	component index
low	low inlet steam concentration
m, n	surface index
o	outgoing
W	wall

INTRODUCTION

Advanced turbines operating in coal-based integrated gasification combined cycle (IGCC) power systems promise higher efficiency and lower emissions [1]. Depending on the fuel type, there are syngas, hydrogen, and oxy-fuel turbines. On the one hand, to improve the thermal efficiency of advanced turbines, the turbine inlet temperature and pressure ratio will be increased to a higher level compared to the conventional natural gas turbine. On the other hand, the working fluid of advanced turbines contains a considerable amount of steam whose thermal properties are fairly different from nitrogen-enriched gas stream in a natural gas turbine [2, 3]. Therefore, there are two major differences between advanced turbines and conventional natural gas turbine: 1) turbine inlet temperature and pressure level and 2) turbine inlet steam concentration. These two sets of parameters together make the aerothermal characteristics of advanced turbines quite different from the conventional gas turbine.

As we know, internal and external cooling technologies are widely used in today's gas turbines to keep the temperature of hot-gas-path components below the material melting temperature limits. The bottom line for turbine cooling system design is the accurate prediction of temperature distribution inside hot-gas-path components based on surface heat loads calculation [4]. Therefore, nearly all of the previous heat-transfer researches on internal and external cooling issues are aimed at providing either qualitative understanding or quantitative correlations that contribute to the accurate prediction of surface heat loads. What's more, these researches for conventional gas turbines are almost conducted at scaled-temperature conditions and the obtained experimental data are typically scaled back to engine flow conditions by designers in their design codes [5]. However, the well developed cooling design database did not take account of the effects of high turbine inlet steam concentration and the increased turbine inlet temperature and pressure levels, and therefore can not be applied directly to advanced turbines in coal-based IGCC systems. For this reason, it is desirable that investigations of turbine inlet steam concentration effects on turbine flow and heat transfer under high-temperature and pressurized conditions should be conducted.

A limited number of researches currently exist in open literature in this subject area. Chyu et al. [2, 3] and Mazzotta et al. [6, 7] described a quantitative comparison of thermal load on the external surface of NASA energy efficient engine (E3) high pressure turbine airfoils between different types of advanced turbines based on computational simulation. They found that the heat transfer coefficients along the airfoil surface were relatively comparable for syngas and hydrogen turbines. However, for the oxy-fuel turbine, the heat transfer coefficient is found to be substantially higher by about $50-60\%$. They also concluded that this is largely caused by the high turbine inlet steam concentration. It is worth mentioning here that they used a simplified radiative heat transfer model in their simulation and proposed that the radiation with an approximately 50% of steam-CO_2 mixture amounts to a $3-5\%$ increase by imposing external heat load on a turbine surface. However, they neglected the feature of film cooling in their study and thus the contribution of radiation was somewhat under-predicted. With basic ideas similar to Chyu et al. [2, 3], Na et al. [8] performed a series of computational simulations to examine the heat transfer and temperature distributions in and about a film-cooled flat plate with the hot-gas flow conditions specified in accordance with the syngas, hydrogen and oxy-fuel turbine operating parameters. The conclusion on turbine inlet steam concentration effects on the aerothermal characteristics of the film-cooled flat plate in this study was similar to Chyu et al. [2, 3]. However, this study neglected radiation modeling in their computational simulation and thus the steam concentration effects were partly under-predicted. Alvin et al. [9] reported an aerothermal test facility being developed by University of Pittsburgh to explore aerothermal cooling of airfoils for use in advanced, land-based, turbine applications. The test rig is a heat transfer testing facility capable of providing realistic turbine flow conditions with elevated temperature and pressure. So far, however, there have been no experimental data reported from this test facility in open literature.

MATHEMATICAL MODEL

In this paper, the authors make an attempt to quantify the effects of gas inlet steam concentration on the aerothermal characteristics of a film-cooled flat plate by means of both experimental and computational approach. As mentioned earlier, the aerothermal difference between advanced turbines and conventional natural gas turbine at similar geometric and flow conditions can be defined by two sets of parameters: 1) turbine inlet temperature and pressure level and 2) turbine inlet steam concentration. Therefore, the main idea of this paper can be described mathematically as the following expression,

$$\Delta \overline{q}'' = \overline{q}''_{high} - \overline{q}''_{low} = f\left(\Delta x_{H_2O,G},\ p_G,\ T_G,\ \frac{X}{D}\right) \tag{1}$$

For clarity, the definition of symbol Δ will be briefly introduced here. As defined in the nomenclature, the symbol Δ represent the change in one quantity from the species with a lower steam concentration to the species with a higher steam concentration at the same inlet pressure and temperature levels. The purpose of this paper is to figure out the above relationship between $\Delta\overline{q}''$ and $\Delta x_{H_2O,G}$ at a fixed geometric and flow condition with a reasonable accuracy. The research in this paper is based on an important assumption that the spanwise-averaged heat flux distribution for turbines with relatively low inlet steam concentration can be predicted by conventional cooling design database, i.e. $\overline{q}''_{low}$ is known beforehand. Therefore, for turbines with higher inlet steam concentrations, if the relation in Eqn. (1) can be figured out, then one can simply add $\Delta\overline{q}''$ obtained in Eqn. (1) to $\overline{q}''_{low}$ so as to correct the conventionally-predicted heat flux distribution. In a word, this paper attempts to correct the conventional cooling design database for advanced turbines with higher inlet steam concentration by figuring out the relation in Eqn. (1).

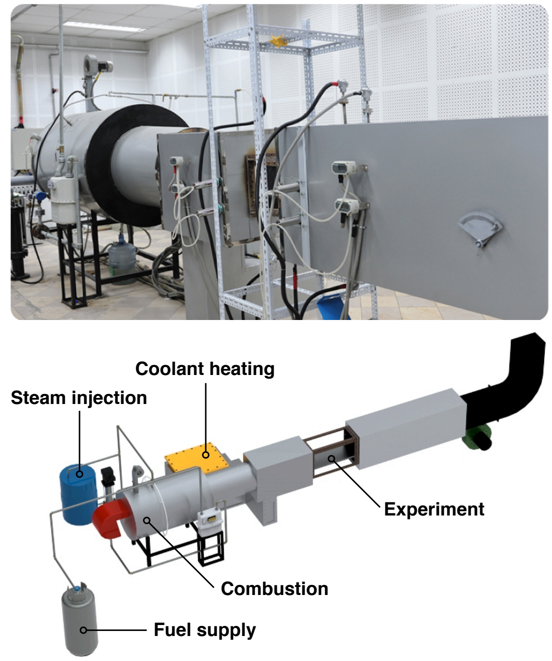

FIGURE 1. **System of experimental facility**

EXPERIMENTAL FACILITY

The experimental method of the present investigation is based on stationary experiments in an open-circuit high-temperature flow system. The photograph and schematic diagram of the installation are shown in Fig. 1. The facility is a high-temperature film-cooling experimental system [10]. The entire experimental system can be divided functionally into six subsystems: fuel supply, combustion, steam injection, coolant heating, experiment and data acquisition. In the gas supply subsystem, the liquefied petroleum gas (LPG) is sent through pipelines to the combustion subsystem. Then the combustor ignites LPG with air from a built-in air pump. Meanwhile, a specified amount of water is pumped from a water tank in the steam injection subsystem to the combustion chamber and mixed with the combustion products to generate a pre-set gas composition or steam concentration. Then the hot gas flows through the flow stabilizer into the test section. In the coolant heating subsystem, air is pumped into an electric heater, heated to a specified temperature and then enters the test section. The most important part of the experiment subsystem is the test section, which will be described in detail later in this section. During the experiment, the data acquisition subsystem monitors all the key experimental parameters, displays primary results on the terminal and records the experiment data with a pre-set frequency.

The test section, as shown in Fig. 2, is a scaled-up film-cooling configuration. The test section is separated into two channels by a nickel-based superalloy flat plate, hot gas channel at the top and coolant channel at the bottom. The working fluid of the hot gas channel is a mixture of steam, carbon dioxide, oxygen and nitrogen, which is generated from LPG combustion and additional steam injection, while the working fluid of coolant channel is electrically-heated air. The inlet steam concentration of the hot gas can be adjusted through the additional steam generator. The inlet temperature of hot gas and coolant channels are maintained at around 800°C and 400°C respectively. The static pressure for the whole test section is maintained at around one atmospheric pressure. The inlet velocities of the hot gas and coolant are both in x-direction, and the designed velocity magnitudes are $20m/s$ and $10m/s$ respectively. Between the two channels, there is a film-cooled flat plate with one row of film-cooling holes inclined at 35 *deg* in streamwise direction. The flat plate is also internally cooled by the coolant beneath.

The primary geometric parameters of the test section are summarized below in Table 1.

The measurement techniques utilized in this paper are briefly introduced in the following part of this section. The inlet velocity and static temperature of the two channels are measured with calibrated water-cooled pitot tubes and high-temperature-resistant thermocouples with measurement error less than 3°C. Surface temperature measurement of the plate is realized by a series of embedded type-K thermocouples with an accuracy of $\pm 0.004 \cdot |t|$. The hot gas inlet composition will be measured with gas chromatography and the obtained gas composition will be

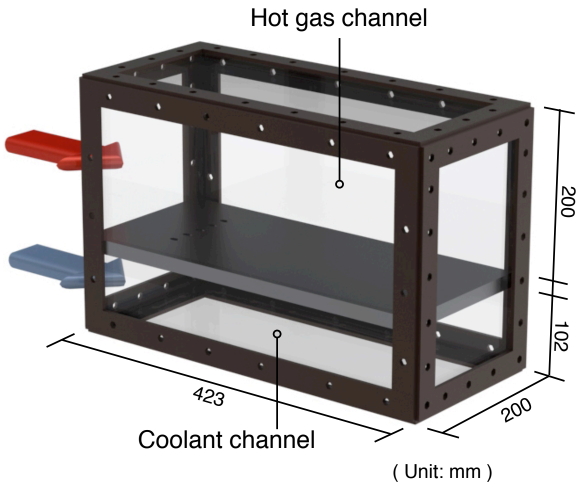

FIGURE 2. **Schematic diagram of test section**

TABLE 1. **Geometric parameters of test section**

Parameter	Hot Gas	Coolant	Flat Plate
$X(mm)$	423	423	423
$Y(mm)$	200	200	200
$Z(mm)$	200	102	18
$D(mm)$	-	-	8
$\alpha(deg)$	-	-	35
$P(mm)$	-	-	24

validated by an online gas analyzer.

COMPUTATIONAL METHOD

The computational method of the present investigation is based on the solving of 3D Reynolds-averaged Navier-Stokes equations with conjugate heat transfer, multi-species and radiation modeling. The main purpose of the computational investigation is to present a viable solution to the modeling of the complex physical problem described in the previous section and then apply this method to study a series of new problems in a wider range of parameters.

Computational Domain and Mesh

To better simulate the real physical problem, the entire test section, including both fluid and solid part, is modeled as the computational domain as shown in Fig. 3. The origin of the coordinate system locates at the hole exit, and the main dimensions of the computational domain have been listed in Table 1.

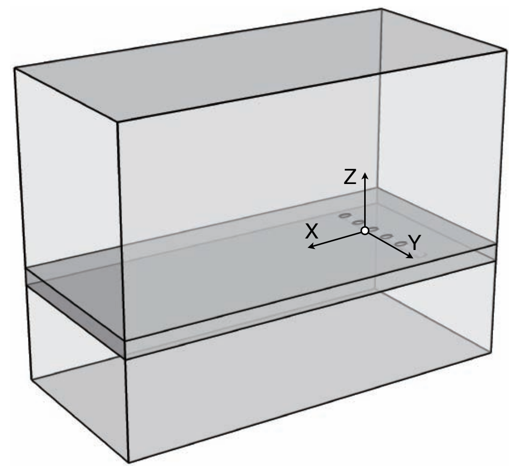

FIGURE 3. **Computational domain**

The computational domain is discretized into 4,100,000 hexahedral cells with the first layer of mesh points away from all viscous walls fulfill the requirement of $y^+ \approx 1$ for the low-Reynolds number $k-\varepsilon$ turbulence model to resolve the laminar sublayer. The spatial discretization is based on a second-order accurate upwind scheme. The local view of the fluid and solid mesh is shown together in Fig. 4.

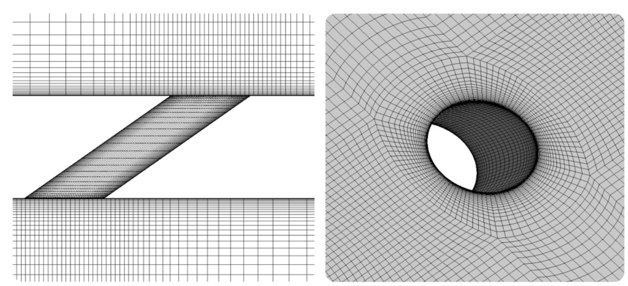

FIGURE 4. **Fluid and solid mesh**

Multi-species Modeling

Multi-species modeling is taken into consideration to simulate the mixing and transport of hot-gas and coolant species. The thermal properties for each component, such as specific heat capacity at constant pressure $c_{p,i}$, thermal conductivity k_i and dynamic viscosity μ_i are computed using kinetic theory, and the corresponding thermal properties for the mixture are computed by means of ideal-gas mixing law. Mass diffusion coefficient D_{ij} between each component is also computed using kinetic theory.

Radiation Modeling

Radiative heat transfer is a very important phenomenon existing in the pre-described problem due to the relatively high steam and carbon dioxide concentrations as well as the high-temperature conditions. In addition to the appropriate use of radiation model, specific treatment with physical significance must also be taken into account to simulate the complex physical nature of radiation with a reasonable accuracy. The following part of this section gives a brief introduction of the radiation modeling issues involved in the simulation.

The discrete ordinates (DO) radiation model is applied to simulate the radiative heat transfer process. All solid walls are treated as opaque, gray and diffuse surface. The absorption coefficient a for the hot gas and coolant is modeled by the weighted-sum-of-gray-gases model (WSGGM) where the local value of a is computed as a function of the local mass fractions of steam and carbon dioxide. In addition, the key to the successful use of DO radiation model is the appropriate treatment of several types of radiative boundary conditions involved in this problem, which are wall boundary conditions and inlet & exit boundary conditions. The radiative wall boundary conditions can be divided into two groups in this study: non-metallic wall and metallic wall. The internal emissivity for non-metallic wall can be approximately specified to the value of 0.9 [11]. Due to lack of accurate measurement of emissivity data for the nickel-based super alloy, the emissivity data of oxidized nickel-chromium alloy at different temperatures is used as an approximation, which is listed in Table 2 [12].

TABLE 2. **Emissivity of nickel-chromium alloy**

Emissivity	$373(K)$	$873(K)$	$1573(K)$
$\varepsilon(T)$	0.87	0.87	0.89

For radiative inlet and exit boundary conditions, the emissivity and black body temperature at each inlet and exit has to be specified appropriately. The two parameters are required to compute the net incident radiant energy at the inlet and exit boundary. In this paper, the authors propose an approximate approach to compute the two parameters based on experimental conditions. To keep this article well-organized, the mathematical details of this approach are described in Appendix A.

Case Setup

Based on the computational method described above, the authors have carried out two group of test cases. First, a validation case to examine the accuracy of the computational model. Second, a series of cases to study the hot-gas inlet steam concentration effects under high-temperature and pressurized conditions. The working conditions for the validation case are mainly taken from measurement but also partly from theoretical calculation, while the working conditions for the second group of cases are specified by the authors for research purpose. The general rule of parameter selection for the second group of cases is to vary hot-gas inlet composition, temperature and pressure independently each for a series of values, while at the same time keep the dimensionless parameters, such as BR, DR, TI_G, Ma_G and Re_G, of all these cases at a comparable level. The parameters of the two groups of cases are summarized in Appendix B.

RESULTS AND DISCUSSION

In this section, results from both experiment and numerical simulations will be presented and discussed. Validation case along with the experimental data will be presented and compared first. Then, numerical investigation on hot-gas inlet steam concentration effects will be presented and analyzed in detail, based on a good agreement of the numerical and experimental results.

Validation Case

To validate the computational models, the authors have carried out a high-temperature film-cooling experiment based on the experimental facility described in the previous section. The main parameters of the experiment are listed in Table 3 and 4. Parameters in Table 3 are measurement results.

TABLE 3. **Experimental parameters for validation case**

Parameter	Hot Gas	Coolant
$T_{inlet}(°\mathrm{C})$	809	416
$V_{inlet}(m/s)$	15	12
$p_{exit}(Pa)$	101408	101427

It is worth mentioning that the data in Table 4 is computed from the enthalpy equilibrium of the equation of combustion due to the difficulty in measuring the components of species accurately. Experimental work on accurate measurement of species fraction is in progress.

In the following part of this section, qualitative results of the validation case will be briefly described before the quantitative comparison with experiment is given.

TABLE 4. Species mole fraction

Mole Fraction (%)	CO_2	H_2O	O_2	N_2
Validation Case	4.23	12.00	12.35	71.42

The near hole flow features shown in Fig. 5 are direct results from numerical simulation, the mixing zone and wake zone contours in Fig. 5 are colored by steam mole fraction and static pressure respectively. As one can see, the simulation well captures the macro flow features of the real problem, including the mixing zone, wake zone and also the well-known counterrotating pair of vortices.

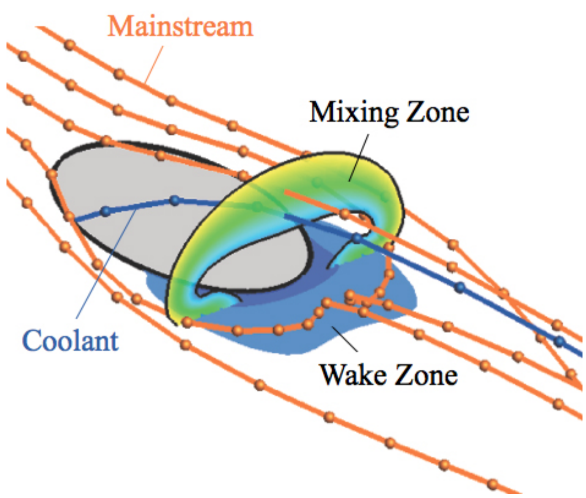

FIGURE 5. Calculated near hole flow features

For completeness, the pressure and temperature contours on the surface of the plate are shown in Fig. 6, which match the simulation results from former researchers.

To fully validate the computational model, not only the qualitative correctness but also the quantitative accuracy are important. The overall cooling effectiveness η versus dimensionless downstream distance X/D from experiment as well as computation are compared in Fig. 7. The experimental data are obtained from thermocouples embedded in the centerline of the plate and for comparison with experiment, the computational data are also extracted from the centerline of plate surface. As one can see, the computational results well predict the trend of centerline η distribution, and also the prediction is quantitatively well with the overall relative error within 1.7%. In further study, more thermocouples will be embedded in the surface of the plate both in spanwise and streamwise direction.

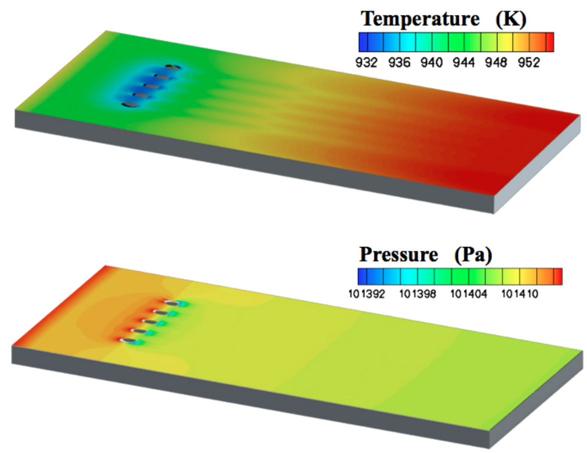

FIGURE 6. Calculated pressure and temperature contours on plate surface

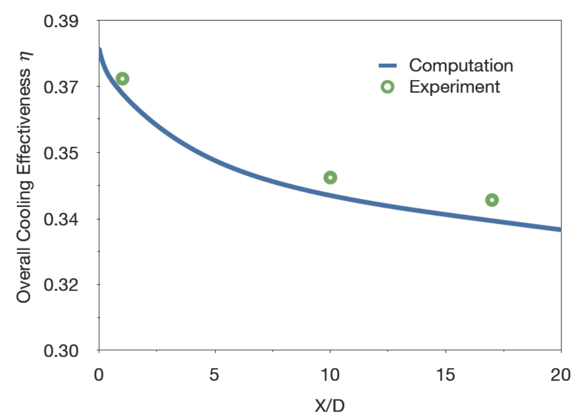

FIGURE 7. Comparison between experiment and computation

The validation case described above shows that the computational models presented in this paper are capable of predicting the investigated problem reasonably well from both qualitative and quantitative perspectives.

Expanded Cases

Based on the validated computational models, a series of expanded test cases were carried out to investigate the influences of inlet steam concentration, as well as inlet pressure and temperature levels, on the aerothermal characteristics of the film-cooled and internally cooled flat plate. The variable parameters selected in this study are hot-gas inlet steam mole fraction, static pressure and static temperature respectively. These parameters are varied in an independent manner, corresponding to totally 45 $(5 \times 3 \times 3)$ test cases. The ranges of these parameters are listed in Table 5.

TABLE 5. Range of varied parameters

Parameter	Range
$x_{H_2O,inlet}$, %	8.50 / 11.08 / 17.30 / 50.00 / 82.00
$p_{static,inlet}$, atm	1.0 / 1.5 / 2.0
$T_{static,inlet}$, °C	800 / 1000 / 1200

As described in the introduction, the authors attempt to figure out the relation in Eqn. (1), i.e. the relation between change in hot-gas inlet steam concentration $\Delta x_{H_2O,G}$ and change in the spanwise-averaged heat flux distribution $\Delta\overline{q}''$, under varied inlet pressure and temperature levels. Before presenting the results in detail, it is necessary to give a concise explanation of the method used for data processing. The baseline species selected for inlet steam concentration are the species with the lowest steam mole fraction at the same inlet pressure and temperature level, and the spanwise-averaged heat flux distribution of all other species will be subtracted by the baseline species to get $\Delta\overline{q}''$ and $\Delta x_{H_2O,G}$. To make the spanwise-averaged heat flux $\Delta\overline{q}''$ dimensionless, area-averaged heat flux $\overline{\overline{q}}''$ from Case1 in Appendix B is selected as an overall heat flux baseline and all the spanwise-averaged heat flux $\Delta\overline{q}''$ will be divided by the baseline heat flux $\overline{\overline{q}}''_{base}$ to get a dimensionless spanwise-averaged heat flux. The baseline for inlet pressure and temperature are selected as the lowest pressure and temperature values in the corresponding parameter range in Table 5. Therefore, the dimensionless form of Eqn. (1) can be obtained,

$$\frac{\Delta\overline{q}''}{\overline{\overline{q}}''_{base}} = g\left(\Delta x_{H_2O,G}, \frac{p_G}{p_{base}}, \frac{T_G}{T_{base}}, \frac{X}{D}\right) \tag{2}$$

All the expanded cases are aiming at figuring out the relation in Eqn. (2).

The following part of this section will give a detailed analysis of the computational data from the expanded cases, including inlet steam concentration effects, inlet pressure influence, inlet temperature influence and also an overall correlation of the data from all the expanded cases.

Steam Concentration Effects Results from the expanded cases show that the variation of inlet steam concentration has little influence on the pressure distribution of plate surface and therefore the flow field. However, heat flux distributions differ a lot between different inlet steam concentration. By processing the data from Case 1-5 in Appendix B to the form presented in Eqn. (2) and getting the logarithm of both sides, the relation between change in steam mole fraction and change in dimensionless area-averaged heat flux can be seen clearly in Fig. 8. The corresponding inlet pressure and temperature for the data shown in Fig. 8 are 1.0atm and 800°C respectively. By correlation, one can get the relation in the following form,

$$\frac{\Delta\overline{q}''}{\overline{\overline{q}}''_{base}} = c_1\left(\Delta x_{H_2O,G}\right)^{c_2} \tag{3}$$

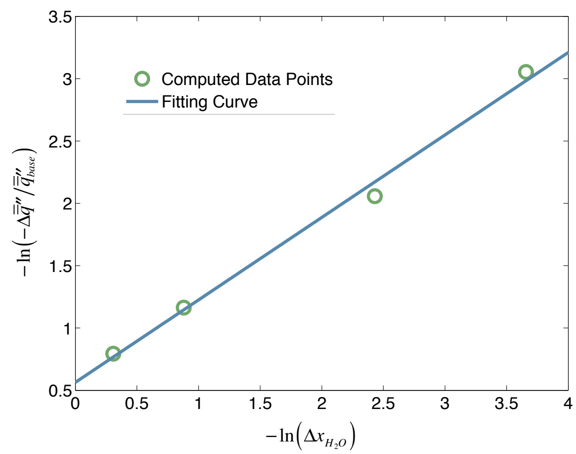

FIGURE 8. Correlation of dimensionless area-averaged heat flux change versus steam concentration change ($p_G = 1.0atm$, $T_G = 800°C$)

Changing the inlet pressure and temperature level will only change the coefficients c_1 and c_2, but not the form of the relation in Eqn. (3), which is shown in Fig. 9.

Therefore, one conclusion can be achieved that the relation between change in gas inlet steam mole fraction $\Delta x_{H_2O,G}$ and change in dimensionless spanwise-averaged heat flux distribution $\Delta\overline{q}''/\overline{\overline{q}}''_{base}$ can be well correlated in the form of a power function, and the correlation coefficients are different under different inlet pressure p_G and inlet temperature T_G.

Inlet Pressure Influence The influence of hot-gas inlet pressure on the relation between $\Delta x_{H_2O,G}$ and dimensionless area-averaged heat flux $\Delta\overline{\overline{q}}''/\overline{\overline{q}}''_{base}$ under different T_G/T_{base} ratios (1.0/1.2/1.4) are shown sequentially in Fig. 10-12. As one can see, when the considered species have relatively small difference from the baseline species in steam concentration, i.e. $\Delta x_{H_2O,G}$ is small, the change in the inlet pressure has little influence on the above relation. However, as the difference in steam concentration $\Delta x_{H_2O,G}$ increased, the influence becomes increasingly evident. To quantify this effect, one can define a pressure influence factor PF as the average growing rate of each curve,

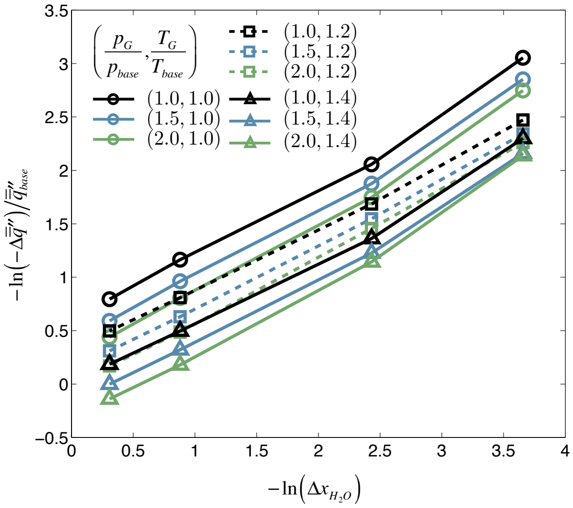

FIGURE 9. Correlation of dimensionless area-averaged heat flux change versus steam concentration change (under different (p_G, T_G))

$$PF = 100 \times \frac{\left(\Delta\bar{\bar{q}}''/\bar{\bar{q}}''_{base}\right)\Big|^{p_G/p_{base}=2.0}_{p_G/p_{base}=1.0}}{(p_G/p_{base})\Big|^{2.0}_{1.0}} \tag{4}$$

The pressure influence factors PF for Fig. 10-12 were computed and listed in Table 6.

TABLE 6. Pressure influence factor

$\Delta x_{H_2O,G}$ (%)	2.58	8.80	41.50	73.50
$T_G/T_{base} = 1.0$	1.69	4.63	13.48	19.27
$T_G/T_{base} = 1.2$	1.98	4.77	16.94	23.57
$T_G/T_{base} = 1.4$	1.75	6.25	22.59	31.97

Conclusion can be made based on the data in Table 6 that the growing rate of $\Delta\bar{\bar{q}}''/\bar{\bar{q}}''_{base}$ with p_G/p_{base} becomes faster as the difference in steam concentration $\Delta x_{H_2O,G}$ is increased with the maximum ratio of growing rate up to a factor of 18.27 (31.97/1.75). Therefore, at high gas inlet steam concentration conditions, the influence of inlet pressure on the aerothermal characteristics of turbine heat transfer is considerable.

Inlet Temperature Influence The influence of hot-gas inlet temperature on the relation between $\Delta x_{H_2O,G}$ and dimensionless area-averaged heat flux $\Delta\bar{\bar{q}}''/\bar{\bar{q}}''_{base}$ under different p_G/p_{base} ratios are shown sequentially in Fig. 13-15. Similar to the influence of inlet pressure, the growing rate of $\Delta\bar{\bar{q}}''/\bar{\bar{q}}''_{base}$ with T_G/T_{base} becomes faster as the difference in steam concentration $\Delta x_{H_2O,G}$ is increased. However, the curves are not as linear as the former ones, which may due to the fourth power law of temperature on radiation heat transfer. Conclusion can also be made that the influence of turbine inlet temperature on the aerothermal characteristics of turbine heat transfer is also considerable at high gas inlet steam concentration conditions.

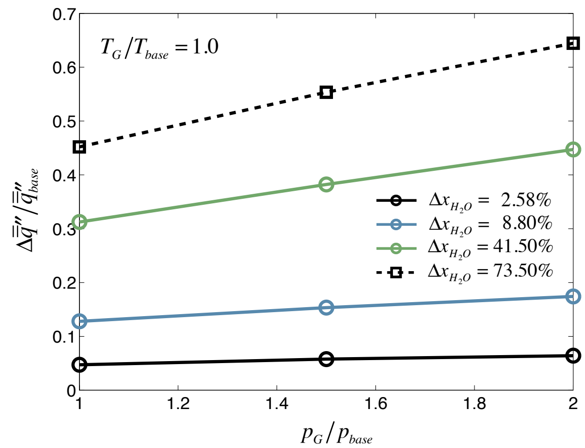

FIGURE 10. Hot-gas inlet pressure influence ($T_G/T_{base} = 1.0$)

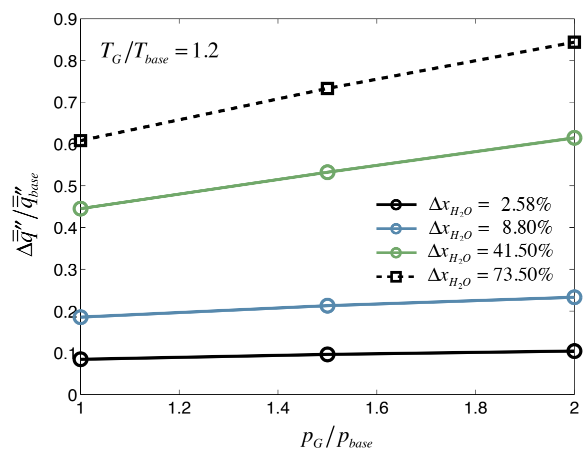

FIGURE 11. Hot-gas inlet pressure influence ($T_G/T_{base} = 1.2$)

Overall Correlation Finally, the authors correlate the data of all the expanded cases into the following equation,

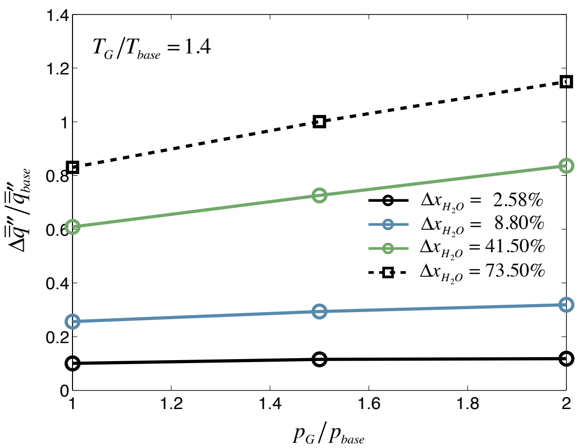

FIGURE 12. **Hot-gas inlet pressure influence** ($T_G/T_{base} = 1.4$)

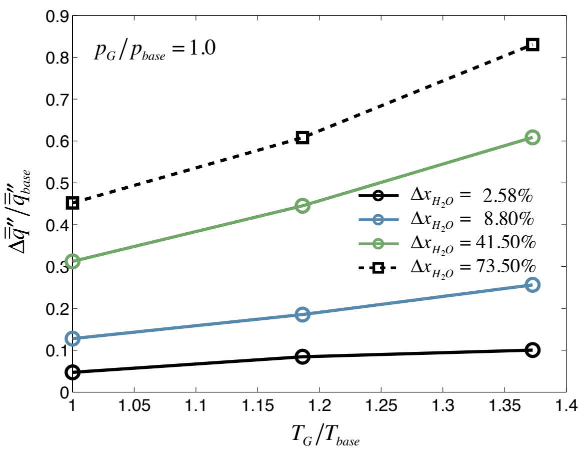

FIGURE 13. **Hot-gas inlet temperature influence** ($p_G/p_{base} = 1.0$)

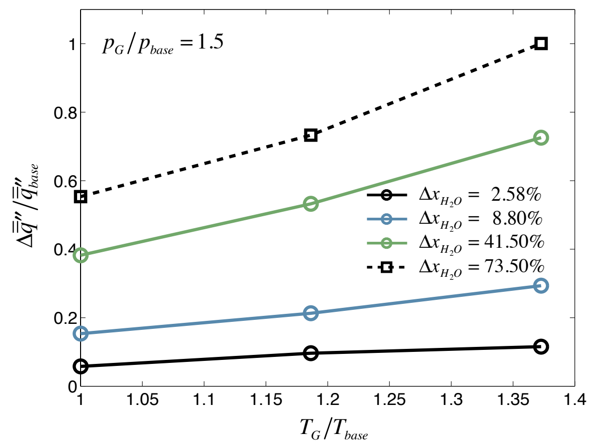

FIGURE 14. **Hot-gas inlet temperature influence** ($p_G/p_{base} = 1.5$)

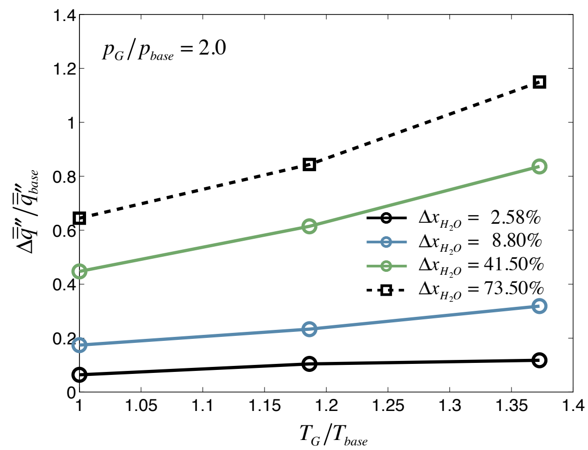

FIGURE 15. **Hot-gas inlet temperature influence** ($p_G/p_{base} = 2.0$)

$$\frac{\Delta\overline{q}''}{\overline{\overline{q}}''_{base}} = c_1\left(\frac{p_G}{p_{base}}, \frac{T_G}{T_{base}}, \frac{X}{D}\right)\left(x_{H_2O,G}\right)^{c_2\left(\frac{p_G}{p_{base}}, \frac{T_G}{T_{base}}, \frac{X}{D}\right)} \quad (5)$$

where the correlation coefficients c_1 and c_2 are second-order nonlinear polynomials on dimensionless pressure p_G/p_{base}, dimensionless temperature T_G/T_{base} and also dimensionless streamwise distance X/D.

To validate the capability of the correlation in Eqn. (5), the authors designed Case 46 in Appendix B. In Fig.16, the spanwise-averaged heat flux distribution results from the correlation in Eqn. (5) are compared with full computational fluid dynamics (CFD) computation. The trend predicted by the correlation agrees quite well with full CFD computation, and the maximum relative error in dimensionless spanwise-averaged heat flux distribution is about 6.3%.

CONCLUSIONS AND RECOMMENDATIONS

This paper conducted an investigation on the influences of turbine inlet steam concentration on turbine flow and heat transfer under high-temperature and pressurized conditions. A high-temperature experimental facility has been built to study the steam concentration effects on turbine aerothermal characteristics for future advanced turbines in IGCC power systems. Preliminary data were obtained from experiment and used to validate the computational models presented in this paper. The computational models involve conjugate heat transfer modeling, multi-species modeling and also radiation heat transfer modeling. Results from computational modeling were compared qualitatively with previous studies and also quantitatively with our

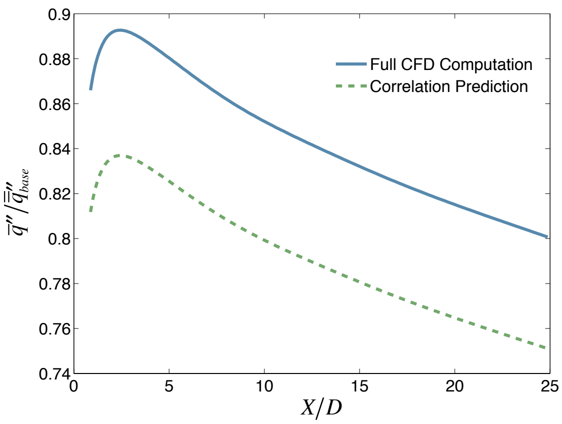

FIGURE 16. **Correlation versus full CFD computation**

experimental measurements, both of which proves the validation of the presented computational approach.

Based on the validated computational models, a series of numerical investigations were conducted. By analyzing the computational data, relation between the change in gas inlet steam concentration and the corresponding change in dimensionless spanwise-averaged heat flux distribution was well correlated with the form of power function. The influence of turbine inlet pressure and temperature on the aerothermal characteristics of turbine heat transfer is also considered and discussed, results show that pressure and temperature effects are considerable only at high steam concentration conditions (with pressure influence factor *PF* up to 18.27). Finally, an overall correlation based on all of the numerical investigations were presented, and the capability of this correlation were validated with full CFD computation. The correlation can predict the trend of the dimensionless spanwise-averaged heat flux quite well, and the maximum relative error is about 6.3% for the predicted case.

As mentioned in earlier sections, this study on the gas inlet steam concentration effects was conducted under fixed geometric and flow conditions. Therefore, all the conclusions were valid under the specific geometric and flow condition. For further studies on gas inlet steam concentration effects, geometric and flow parameters can be varied to a different level, e.g. higher blowing ratios, to get a more general conclusion. Another recommendation for future study is that experimental data instead of numerical simulation results should be employed in the correlation of Eqn. (1) or (2).

ACKNOWLEDGMENT

The work was partly supported by the National Natural Science Foundation of China (Grant No. 50676043) and the Special Funds for Major State Basic Research Projects (Grant No. 2007CB210108).

REFERENCES

[1] Dennis, R. A., and Harp, R., 2007. "Overview of the u.s. department of energy's office of fossil energy advanced turbine program for coal based power systems with carbon capture". *ASME Conference Proceedings,* ***2007***(47918), pp. 1093–1104.

[2] Chyu, M. K., Mazzotta, D. W., Siw, S. C., Karaivanov, V. G., Slaughter, W. S., and Alvin, M. A., 2009. "Aerothermal challenges in syngas, hydrogen-fired, and oxyfuel turbines—part i: Gas-side heat transfer". *Journal of Thermal Science and Engineering Applications,* ***1***(1), p. 011002.

[3] Chyu, M. K., Siw, S. C., Karaivanov, V. G., Slaughter, W. S., and Alvin, M. A., 2009. "Aerothermal challenges in syngas, hydrogen-fired, and oxyfuel turbines—part ii: Effects of internal heat transfer". *Journal of Thermal Science and Engineering Applications,* ***1***(1), p. 011003.

[4] Moffat, R. J., 1987. "Turbine blade heat transfer". In *Heat Transfer and Fluid Flow in Rotating Machinery*, Yang, ed. Hemisphere, Washington, D. C., pp. 1–24.

[5] Han, J. C., Dutta, S., and Ekkad, S. V., 2000. *Gas Turbine Heat Transfer and Cooling Technology*. Taylor & Francis, New York.

[6] Mazzotta, D. W., Karaivanov, V. G., Chyu, M. K., Slaughter, W. S., and Alvin, M. A., 2008. "Gas-side heat transfer in syngas, hydrogen-fired and oxy-fuel turbines". *ASME Conference Proceedings,* ***2008***(43147), pp. 1815–1825.

[7] Mazzotta, D. W., Chyu, M. K., and Alvin, M. A., 2007. "Airfoil heat transfer characteristics in syngas and hydrogen turbines". *ASME Conference Proceedings,* ***2007***(47926), pp. 793–801.

[8] Na, S., Dennis, R. A., Alsup, C., Bryden, K. M., and Shih, T. I.-P., 2009. "Effects of hot-gas composition on temperature distribution in a flat plate cooled by internal and film cooling". *ASME Conference Proceedings,* ***2009***(48845), pp. 657–668.

[9] Alvin, M. A., Pettit, F., Meier, G., Yanar, N., Chyu, M., Mazzotta, D., Slaughter, W., Karaivanov, V., Kang, B., Feng, C., Chen, R., and Fu, T. C., 2007. "Materials and component development for advanced turbine systems". In 5th International Conference on Advances in Materials Technology for Fossil Power Plants.

[10] Wang, W., Zou, X., Sun, P., Lin, Z., Ren, J., Yuan, X., and Jiang, H., 2010. "Experimental and numerical investigation on a flat plate with film cooling". *Journal of Tsinghua University,* ***50***(12), pp. 1988–1993.

[11] Yang, S., and Tao, W., 2006. *Heat Transfer*. Higher Education Press, Beijing.

[12] OMEGASCOPE. Table of Emissivity. See also URL http://www.omega.com/temperature/z/pdf/z088-089.pdf.

[13] Modest, M. F., 2003. *Radiative Heat Transfer*. An imprint of Elsevier Science, San Diego, California.

Appendix A: Mathematical Model for Radiative Inlet and Exit Boundary Conditions

This section describes the mathematical model used in this paper to compute emissivity at radiative inlet and exit boundary conditions. Demonstration of this approach will be given based on the hot-gas inlet boundary, since the computation process is quite similar for other radiative inlet or exit boundary conditions. For simplicity, the gas temperature in flow stabilizer is assumed to be equal to the gas inlet temperature for the test section, therefore the black body temperature is also equal to the hot gas inlet temperature. Another important assumption is made that the radiant energy entering the hot-gas inlet boundary is totally from the flow stabilizer section as shown in Fig. 17. The total radiant energy can be calculated using the gray gas in gray enclosure model, in which the average emissivity of gases can be obtained using the procedure provided by [13].

Gray Gas in Gray Enclosure Model

The authors assume that the flow stabilizer is a closed cavity whose interior walls can be treated as gray body, i.e. the emissivity of each interior wall is constant. According to the gray gas in gray enclosure model for closed cavity, the following set of equations can be obtained,

$$\frac{Q_{i,m}}{A_m} = \sum_{n=1}^{N_m} \left(\frac{Q_{o,n}}{A_n} F_{m-n} \overline{\tau}_{n-m} + e_{b,g} F_{m-n} \overline{\alpha}_{n-m} \right) \tag{6}$$

One more approximation can be made from experimental conditions, which is $T_1 = T_2 = T_3 \approx T_G$. Based on the above approximations, solution of the set of equations in Eqn. (6) can be obtained, provided the average emissivity of gases is calculated beforehand.

Average Emissivity of Gases

As described in the previous subsection, to compute the radiant energy contribution from the flow stabilizer to the hot-gas inlet boundary, the average emissivity of gases to the this boundary is needed. Therefore, methods for computing the average emissivity of gases to its surrounding walls are described in the following part of this section.

The only two components of the gases in flow stabilizer that contribute to radiation heat transfer are steam and carbon dioxide, therefore, the average emissivity of gases to its surrounding walls can be obtained according to the procedure provided by [13],

$$\varepsilon_{CO_2+H_2O} = \varepsilon_{CO_2} + \varepsilon_{H_2O} - \Delta\varepsilon\left(p_{H_2O}L, p_{CO_2}L\right) \tag{7}$$

$$\varepsilon_i\left(p_iL, p, T_G\right) = \varepsilon_{0i}\left(p_iL, 1bar, T_G\right) \left(\frac{\varepsilon}{\varepsilon_0}\right)_i \left(p_iL, p, T_G\right),\ i = CO_2,\ H_2O \tag{8}$$

where,

$$\varepsilon_0\left(p_aL, p = 1bar, T_G\right) = exp\left[\sum_{i=0}^{M}\sum_{j=0}^{N} c_{ji} \left(\frac{T_G}{T_0}\right)^j \left(log_{10}\frac{p_aL}{(p_aL)_0}\right)^i\right] \tag{9}$$

$$\frac{\varepsilon\left(p_aL, p, T_G\right)}{\varepsilon_0\left(p_aL, 1bar, T_G\right)} = 1 - \frac{(a-1)(1-P_E)}{a+b-1+P_E} exp\left(-c\left[log_{10}\frac{(p_aL)_m}{p_aL}\right]^2\right) \tag{10}$$

$$\Delta\varepsilon = \left[\frac{\zeta}{10.7+101\zeta} - 0.0089\zeta^{10.4}\right]\left(log_{10}\frac{(p_{H_2O}+p_{CO_2})L}{(p_aL)_0}\right)^{2.76} \tag{11}$$

The coefficients and nomenclature of the above formulas are neglected here, which can also be found in reference [13].

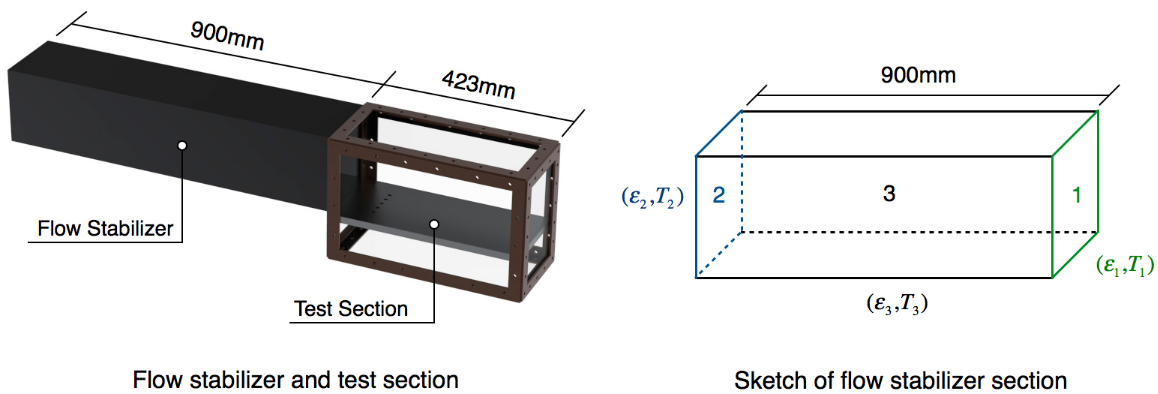

FIGURE 17. **Illustration of radiative inlet and exit boundary condition modeling**

Appendix B: Case Matrix

TABLE 7. **Species mole fraction**

Mole Fraction (%)	CO_2	H_2O	O_2	N_2	Ar
Validation	4.23	12.00	12.35	71.42	0.00
Species1	9.27	8.50	8.63	72.80	0.80
Species2	5.66	11.08	8.60	74.66	0.00
Species3	1.40	17.30	8.20	72.20	0.90
Species4	5.20	50.00	2.96	41.84	0.00
Species5	16.00	82.00	0.10	1.10	0.80
Species6	4.6	30.00	8.04	57.36	0.00

TABLE 8: **Case Matrix**

Case	Species	$p_G(atm)$	T_G(°C)	Re_G	$TI_G(\%)$	Ma_G	DR	BR	VR
1	Species1	1.0	800	1.57×10^5	3.6	0.16	1.44	0.23	0.16
2	Species2	1.0	800	1.53×10^5	3.6	0.16	1.41	0.24	0.17
3	Species3	1.0	800	1.46×10^5	3.6	0.15	1.41	0.24	0.17
4	Species4	1.0	800	1.34×10^5	3.7	0.15	1.47	0.25	0.17
5	Species5	1.0	800	1.28×10^5	3.7	0.14	1.50	0.24	0.16
6	Species1	1.5	800	2.35×10^5	3.4	0.16	1.44	0.23	0.16
7	Species2	1.5	800	2.29×10^5	3.4	0.16	1.41	0.24	0.17
8	Species3	1.5	800	2.19×10^5	3.4	0.15	1.47	0.25	0.17
9	Species4	1.5	800	2.01×10^5	3.5	0.15	1.44	0.26	0.18
10	Species5	1.5	800	1.93×10^5	3.5	0.14	1.53	0.26	0.17
11	Species1	2.0	800	3.14×10^5	3.3	0.16	1.44	0.23	0.16
12	Species2	2.0	800	3.05×10^5	3.3	0.16	1.41	0.24	0.17
13	Species3	2.0	800	2.92×10^5	3.3	0.15	1.47	0.25	0.17
14	Species4	2.0	800	2.68×10^5	3.4	0.15	1.50	0.27	0.18
15	Species5	2.0	800	2.57×10^5	3.4	0.14	1.50	0.27	0.18
16	Species1	1.0	1000	1.30×10^5	3.7	0.16	1.44	0.23	0.16
17	Species2	1.0	1000	1.26×10^5	3.7	0.16	1.44	0.23	0.16
18	Species3	1.0	1000	1.20×10^5	3.7	0.15	1.41	0.24	0.17
19	Species4	1.0	1000	1.09×10^5	3.8	0.15	1.41	0.24	0.17
20	Species5	1.0	1000	1.03×10^5	3.8	0.14	1.44	0.23	0.16
21	Species1	1.5	1000	1.95×10^5	3.5	0.16	1.44	0.23	0.16
22	Species2	1.5	1000	1.89×10^5	3.5	0.16	1.41	0.24	0.17
23	Species3	1.5	1000	1.81×10^5	3.5	0.15	1.47	0.25	0.17
24	Species4	1.5	1000	1.64×10^5	3.6	0.15	1.53	0.26	0.17
25	Species5	1.5	1000	1.54×10^5	3.6	0.14	1.53	0.26	0.17
26	Species1	2.0	1000	2.59×10^5	3.4	0.16	1.44	0.23	0.16
27	Species2	2.0	1000	2.52×10^5	3.4	0.16	1.50	0.24	0.16
28	Species3	2.0	1000	2.41×10^5	3.4	0.15	1.47	0.25	0.17
29	Species4	2.0	1000	2.18×10^5	3.4	0.15	1.50	0.27	0.18
30	Species5	2.0	1000	2.05×10^5	3.5	0.14	1.50	0.27	0.18

to be continued

TABLE 8: **Case Matrix (continued)**

Case	Species	$p_G(atm)$	$T_G(°\mathrm{C})$	Re_G	$TI_G(\%)$	Ma_G	DR	BR	VR
31	Species1	1.0	1200	1.11×10^5	3.7	0.16	1.38	0.22	0.16
32	Species2	1.0	1200	1.08×10^5	3.8	0.16	1.44	0.23	0.16
33	Species3	1.0	1200	1.03×10^5	3.8	0.16	1.35	0.23	0.17
34	Species4	1.0	1200	0.92×10^5	3.8	0.15	1.44	0.23	0.16
35	Species5	1.0	1200	0.86×10^5	3.9	0.15	1.47	0.22	0.15
36	Species1	1.5	1200	1.67×10^5	3.6	0.16	1.38	0.22	0.16
37	Species2	1.5	1200	1.62×10^5	3.6	0.16	1.44	0.23	0.16
38	Species3	1.5	1200	1.54×10^5	3.6	0.16	1.41	0.24	0.17
39	Species4	1.5	1200	1.38×10^5	3.6	0.15	1.47	0.25	0.17
40	Species5	1.5	1200	1.29×10^5	3.7	0.15	1.47	0.25	0.17
41	Species1	2.0	1200	2.22×10^5	3.4	0.16	1.38	0.22	0.16
42	Species2	2.0	1200	2.16×10^5	3.4	0.16	1.44	0.23	0.16
43	Species3	2.0	1200	2.05×10^5	3.5	0.16	1.41	0.24	0.17
44	Species4	2.0	1200	1.84×10^5	3.5	0.15	1.53	0.26	0.17
45	Species5	2.0	1200	1.72×10^5	3.5	0.15	1.53	0.26	0.17
46	Species6	1.0	800	1.43×10^5	3.6	0.15	1.50	0.24	0.16
47	Validation	1.0	809	0.22×10^5	4.6	0.02	1.43	0.87	0.61